



TITLE:

Adaptive Cation Pillar Effects Achieving High Capacity in Li-Rich Layered Oxide, LiMnO-LiMeO (Me = Ni, Co, Mn)

AUTHOR(S):

Hiroi, Satoshi; Oishi, Masatsugu; Ohara, Koji; Shimoda, Keiji; Kabutan, Daiki; Uchimoto, Yoshiharu

CITATION:

Hiroi, Satoshi ...[et al]. Adaptive Cation Pillar Effects Achieving High Capacity in Li-Rich Layered Oxide, LiMnO-LiMeO (Me = Ni, Co, Mn). *Small* 2022, 18(42): 2203412.

ISSUE DATE:

2022-10-20

URL:

<http://hdl.handle.net/2433/276824>

RIGHT:

© 2022 The Authors. *Small* published by Wiley-VCH GmbH; This is an open access article under the terms of the Creative Commons Attribution License, which permits use, distribution and reproduction in any medium, provided the original work is properly cited.

Adaptive Cation Pillar Effects Achieving High Capacity in Li-Rich Layered Oxide, $\text{Li}_2\text{MnO}_3\text{-LiMeO}_2$ (Me = Ni, Co, Mn)

Satoshi Hiroi,* Masatsugu Oishi,* Koji Ohara,* Keiji Shimoda, Daiki Kabutan, and Yoshiharu Uchimoto

Intensive research is underway to further enhance the performance of lithium-ion batteries (LIBs). To increase the capacity of positive electrode materials, Li-rich layered oxides (LLO) are attracting attention but have not yet been put to practical use. The structural mechanisms through which LLO materials exhibit higher capacity than conventional materials remain unclear because their disordered phases make it difficult to obtain structural information by conventional analysis. The X-ray total scattering analysis reveals a disordered structure consisting of metal ions in octahedral and tetrahedral sites of Li layers as a result of cation mixing after the extraction of Li ions. Metal ions in octahedral sites act as rigid pillars. The metal ions move to the tetrahedral site of the Li layer, which functions as a Li-layer pillar during Li extraction, and returns to the metal site during Li insertion, facilitating Li diffusion as an adaptive pillar. Adaptive pillars are the specific structural features that differ from those of the conventional layered materials, and their effects are responsible for the high capacity of LLO materials. An essential understanding of the pillar effects will contribute to design guidelines for intercalation-type positive electrodes for next-generation LIBs.


1. Introduction

Lithium-rich layered oxide (LLO) has attracted attention as a next-generation positive electrode material for lithium-ion

S. Hiroi, K. Ohara
Diffraction and Scattering Division
Japan Synchrotron Radiation Research Institute (JASRI)
1-1-1 Kouto, Sayo-cho, Sayo-gun, Hyogo 679-5198, Japan
E-mail: s_hiroi@spring8.or.jp; ohara@spring8.or.jp

M. Oishi, D. Kabutan
Graduate School of Technology
Industrial and Social Sciences
Tokushima University
2-1 Minami Josanjima-cho, Tokushima 770-8506, Japan
E-mail: ooishi.masatsugu@tokushima-u.ac.jp

K. Shimoda
Office of Society-Academia Collaboration for Innovation
Kyoto University
Gokasho, Uji, Kyoto 611-0011, Japan
Y. Uchimoto
Graduate School of Human and Environment Studies
Kyoto University
Yoshida Nihonmatsu-cho, Sakyo-ku, Kyoto 606-8501, Japan

 The ORCID identification number(s) for the author(s) of this article can be found under <https://doi.org/10.1002/smll.202203412>.

© 2022 The Authors. Small published by Wiley-VCH GmbH. This is an open access article under the terms of the Creative Commons Attribution License, which permits use, distribution and reproduction in any medium, provided the original work is properly cited.

DOI: 10.1002/smll.202203412

batteries, not only because of its high discharge capacity but also because of its unique mechanism of charge compensation and structural changes associated with the extraction and insertion of Li ions. LLO is commonly represented as a composite material of the Li_2MnO_3 host structure mixed with the layer-structure LiMeO_2 (Me = Ni, Co, Mn). LLO exhibits a reversible discharge capacity above 250 mAh g^{-1} , suggesting that about 1 mol of Li ions are reversibly extracted from and inserted into the positive electrode;^[1–5] this is limited to about 0.6 mol of Li ions (about 160 mAh g^{-1}) in a conventional layered oxide such as LiCoO_2 . The LLO electrode exhibits specific charge and discharge profiles indicating that the initial charge process shows a voltage gradient of up to $\approx 4.5 \text{ V}$, followed by an irreversible potential plateau process.^[6–9] Charge compensation is achieved by a redox reaction

of transition metals in the potential gradient region and by oxygen reactions (O^{2-}/O^- redox couple and/or O_2 release) in the potential plateau.^[7–18]

To some extent, researchers have a common understanding of the charge compensation mechanism of LLO materials that the de/lithiation reactions are charge-compensated by contributions from both the metal cation and oxygen anion. On the other hand, there are various reports on structural changes accompanying de/lithiation reactions, but there is little consensus among researchers on structural mechanisms. For example, it is still not clear whether a pristine structure is a two-phased mixture of Li_2MnO_3 and LiMeO_2 (Me = Ni, Co, Mn) or a single phase of the solid solution of the two.^[19–27] In the single-phase structure model, Li ions should be extracted uniformly from one entire structure. On the other hand, in the composite structure model, Li ions are expected to be extracted from the LiMeO_2 domain in the potential gradient region and then from the Li_2MnO_3 domain in the voltage plateau region. The crystal structures of LLO materials have been examined by Rietveld analysis, which is widely used for structural analysis of crystalline materials. On the basis of the results of Rietveld refinements from neutron diffraction data, Idemoto et al.^[28] reported that $\text{Li}(\text{Li}_{1/6}\text{Mn}_{1/2}\text{Ni}_{1/6}\text{Co}_{1/6})\text{O}_2$ has the Li_2MnO_3 -type layered structure ($C2/m$), and Ni and Co occupy both the 4g and 2b sites in the transition metal layer. From a pair distribution function (PDF) analysis of neutron total scattering data, they also reported that the structural disorder of the transition metal layer differs depending on the composition ratio of

Ni, Mn, and Co elements, which cannot be confirmed by the average structural analysis.^[29] On the basis of the results of Rietveld analysis using X-ray diffraction (XRD) data, Amalraj et al. reported^[30] that the structure of the $x\text{Li}_2\text{MnO}_3 \cdot (1-x)\text{Li}(\text{Mn, Ni, Co})\text{O}_2$ pristine material is a two-phase system consisting of structurally integrated layered monoclinic Li_2MnO_3 ($C2/m$) and rhombohedral LiMO_2 ($R\bar{3}m$) components. Kleiner et al.^[31] mentioned that it is not possible to determine whether LLO materials are a single-phase material or a composite from XRD data, although they refined the in situ synchrotron XRD results to reveal a single-phase structure of $R\bar{3}m$ and suggested that the transition metal moves to the tetrahedral site of the Li layer as Li ions are removed and returns to the octahedral site of the original transition metal layer when Li ions are inserted. A wide variety of results have been reported for LLO materials; however, it is a common understanding that LLO exhibits an irreversible reaction during the initial charge process, as is clear from the charge–discharge curve. Furthermore, the new structure obtained after the irreversible reaction that realizes a high capacity in the subsequent cycles is still unclear.

Cation mixing during the cycling process is one of the specific characteristics recognized in LLO materials. Shimoda et al.^[18] reported that the pristine state of LLO is a composite structure of Ni-free and Ni-containing Li_2MnO_3 and LiMeO_2 nanodomains, and after the initial charge, the layered rock-salt structure and the Li_2MnO_3 phase having a partial spinel structure are formed by cation mixing. After the subsequent discharge process, the cation mixing results in a domainless layered structure, and the Li ions are extracted from and inserted into the newly obtained single-phase structure. Yin and Tarascon et al. reported^[32] that upon further oxidation above the conventional cut-off voltage of 4.8 V during the initial charge process in $x\text{Li}_2\text{MnO}_3 \cdot (1-x)\text{Li}(\text{Mn, Ni, Co})\text{O}_2$, Mn migration is triggered by the anionic redox activity, and the Mn ions at interlayer Li sites may act as pillars for the layered structures. The formation of the spinel phase in LLO materials has often been discussed.^[30,33–36] The spinel phase, which has the same cubic close-packed oxygen arrangement as LLO, can be formed by cation migrations during the extraction of Li ions. However, the spinel phase formed in the charged LLO does not have a simple spinel structure, as its electrochemical properties are different from those of spinel electrodes. Problems obstructing the practical usage of LLO, such as the voltage decay and cycle degradation caused by the irreversible diffusion of metal ions into the octahedral sites of Li layers and the spinel formation associated with the migration of metal ions to tetrahedral sites, have been recognized.

Many review papers on LLO materials have been reported,^[33,37–42] which commonly deal with the drawbacks of the LLO material that prevent its practical usage. In them, structural instability, low kinetics, inefficient voltage decay, and low initial coulombic efficiency have been discussed. Further, the degeneration occurring on the LLOs particle surface is also reported.^[43,44] These review papers commonly present that the structural change is caused by the migration of transition metals associated with Li and oxygen desorption, and powder process designs, surface treatments, interfacial side reaction, and doping of different elements are reported as remedial measures. However, the structural mechanism through which large

amounts of Li ions are desorbed and inserted, an inherently excellent feature of this LLO material, has not been discussed in detail. The reasons are the presence of disordered phases of LLO after the initial charge and the difficulty in revealing their details from a conventional average structure analysis using XRD. Local atomic structure analyses such as X-ray absorption spectroscopy (XAS) and transmission electron microscopy (TEM) have been conducted to reveal the disordered phases of LLO, but these methods have different analytical ranges and limited observation methods; hence, a variety of results have been reported. Until now, the structural mechanism that can explain the high capacity of LLO materials has not yet been clarified. In addition, the superoxide and peroxide ion-like states observed during charging are not found within the crystal structure of layered oxides and may be formed in a structure with low symmetry or a disordered structure. Ceder's group^[43] reported that the disordered lithium transition metal oxides with the rock-salt structure are a new type of positive electrode of high-energy-density lithium-ion batteries that achieve reversible anion redox reactions. We have performed combinations of XRD, TEM, XAS, and PDF analyses to comprehensively reveal the disordered crystal structure of the Li_2MnO_3 electrode.^[44] XRD and TEM analysis showed the formation of a low crystalline phase, and XAS and PDF analysis showed that the MnO_6 -based framework is rearranged after initial charging while maintaining octahedral coordination. The structural information of the low-crystallinity disorder phase was visualized on the basis of the difference PDF, and it was shown that the Li-poor phase has a structure similar to that of cubic spinel LiMn_2O_4 , not delithiated LiMn_2O_4 ($\lambda\text{-MnO}_2$). In other words, after the initial charge, Mn occupancy is disordered in the Li-poor phase owing to Mn migration to the Li vacancy sites.^[40] In addition, the medium-range order in the Li-poor phase is disordered, and the coherent domain size is on the order of 1 nm. Thus, the composite structure formed after the initial charge consists of a disordered cubic spinel structure and unreacted Li_2MnO_3 phases. Uncovering the structural modifications associated with the desorption and insertion of Li ions, undetectable by average structure analysis, is required to determine the excellent properties of this composite material. The PDF obtained by X-ray total scattering measurement enables the quantitative and simultaneous determination of the average and disordered structures due to its high real-space resolution. PDF analysis is the most appropriate method for LLO materials, which are assumed to undergo local structural changes while maintaining a certain degree of the layered host structure. For PDF analysis, in situ measurement is reported,^[45] though we chose ex situ measurements to probe only cathode material samples as LLO materials are known to undergo complex structural changes.

In this study, X-ray total scattering measurements of a practical LLO electrode, $\text{Li}_{1.16}\text{Ni}_{0.15}\text{Co}_{0.19}\text{Mn}_{0.50}\text{O}_2$, were performed, and the average and local structure variations during charging and discharging were evaluated by PDF analysis. First, the pristine structure of the composite material was analyzed in detail. Then, the new structure obtained after the initial charging process was evaluated. Two types of transition metal ions that show different pillar effects were identified whereby extraction and insertion of large amounts of Li ions in LLO materials were realized.

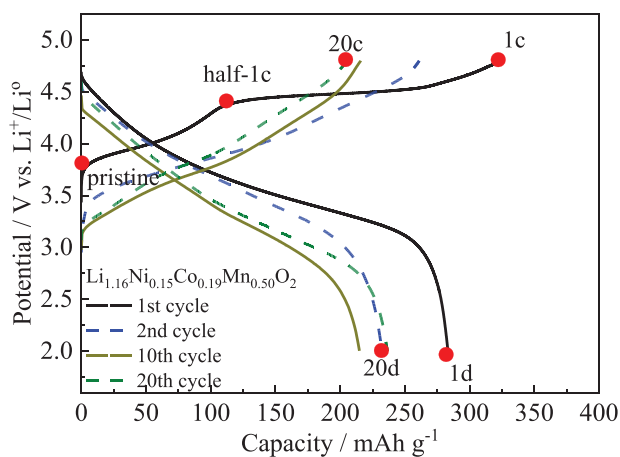


Figure 1. Charge–discharge profiles of $\text{Li}_{1.16}\text{Ni}_{0.15}\text{Co}_{0.19}\text{Mn}_{0.50}\text{O}_2$.

2. Results and Discussion

Figure 1 shows the charge–discharge profiles of the $\text{Li}_{1.16}\text{Ni}_{0.15}\text{Co}_{0.19}\text{Mn}_{0.50}\text{O}_2$ electrode. The first charge capacity reached 330 mAh g^{-1} ; However, the capacity of the subsequent cycles after the irreversible charge decreased to 280 mAh g^{-1} . A voltage plateau typical of LLO materials was observed after the half charge state of the first charge process. The irreversible voltage plateau in the first charge process was not observed thereafter. The profile of the first charge indicated the existence of two reactions. X-ray total scattering measurements were performed in the pristine, first half-charged state before the voltage plateau, first charged, first discharged, and 20th charged and discharged states to characterize the structural changes due to the charge–discharge process.

Figure 2a) shows the XRD profile of the pristine $\text{Li}_{1.16}\text{Ni}_{0.15}\text{Co}_{0.19}\text{Mn}_{0.50}\text{O}_2$. The diffraction peaks can be indexed with the space group $R\bar{3}m$ except for the additional superlattice peaks of $C2/m$. Thus, the pristine material is identified as a single $C2/m$ structure phase ($\text{Li}_{1.16}\text{Ni}_{0.15}\text{Co}_{0.19}\text{Mn}_{0.50}\text{O}_2$) or a mixture of phases of $C2/m$ and $R\bar{3}m$ structures ($0.3\text{Li}_2\text{MnO}_3 + 0.7\text{Li}(\text{Ni}_{1/3}\text{Co}_{1/3}\text{Mn}_{1/3})\text{O}_2$). Yu et al.^[21] reported two phases of the integrated LiMeO_2 (Me = Ni, Co, and Mn) and Li_2MnO_3 -like structures in an LLO material, determined by scanning transmission electron microscopy (STEM). Thackeray et al.^[2] reported that the crystal structure of the LLO material containing Co ions is extremely complex, and the introduction of Co^{3+} ions would enhance the disorder and isolation of the LiMe_6 cation region. Hence, it is difficult to observe the short-range order in the LLO structure. PDF analysis is useful for elucidating the complex structure of an LLO material containing Co ions. The detailed results of our PDF analysis of whether the pristine structure is a single phase or multiple phases are shown later. The experimental $S(Q)$ curves are shown in Figure S1 (Supporting Information), and enlarged superlattice peaks are shown in Figure 2b). The superlattice peaks were observed in the pristine and half-charged materials. After the first charge at 4.8 V, only the peak profile from the $R\bar{3}m$ structure was recognized. This indicates that the $C2/m$ structure derived from the Li_2MnO_3 phase was lost between the half-charged and first charge states. The Bragg peak profile attributed to $R\bar{3}m$ was

observed in both charged and discharged states (Figure S1, Supporting Information). However, atomic occupancy and the other structural parameters were expected to be different because the Bragg peak intensity ratios were not the same between the charged and discharged states.

Figure 2c,d shows the $G(r)$ curves of the electrode samples. The first Me–O and second Me–Me peaks at 1.90 and 2.85 Å indicate an octahedral MeO_6 structure (Me = Ni, Co, and Mn) in the $C2/m$ and $R\bar{3}m$ structures. The first Me–O peak intensity was almost unchanged regardless of the charge state of the samples, suggesting a sturdy MeO_6 octahedron in the metal layer. On the other hand, the amplitude of $G(r)$ was weakened beyond the first peak by the first delithiation. The results show that local disorders, such as cation mixing, were introduced into the crystal in the charged state. The $G(r)$ oscillation recovered in the first discharged state, although the intensity was lower than that in the pristine state. This lower intensity indicates the mixing of the remaining transition metals even in the discharged state. The third peak, around 3.5 Å, is the superposition of the Me–Li tetrahedral site and the second neighbor Me–O correlation.^[46] The peak was slightly shifted and enhanced in the charged states. This enhanced peak suggested a leakage of the transition metals into the Li tetrahedral site upon charging. The shifted peak position reflected a variation of the lattice constant or shorter correlation of the Me–Li tetrahedral site compared to the second Me–O.

Considering the charge compensation of this material, contributions by the oxygen anion in addition to metal cations is considered. We reported the redox reactions of both oxygen anion and metal cations charge compensating the de/lithiation by XAS.^[6,7] Hence, the oxygen anion is oxidized in the charge samples evaluated in this study. However, we could not confirm from the $G(r)$ profiles that indicate the short O–O correlations formed by the oxidation of oxygen anions (Figure S1, Supporting Information). This is because the short-range correlations of light elements are difficult to distinguish using X-rays, and moreover similar length of correlations of carbon used as a conductive agent also exists in the samples.

The structural parameters of the materials were refined by the procedure described in the previous section using $G(r)$. The adequacy of the calculation conditions considered in the structural analysis, such as crystal structure, chemical composition, and occupancy, was examined. The composition of the pristine sample was determined by inductively coupled plasma-atomic emission spectroscopy (ICP-AES) to be $\text{Li}_{1.16}\text{Ni}_{0.15}\text{Co}_{0.19}\text{Mn}_{0.50}\text{O}_2$. Considering the delivered capacities neglecting possible contributions from side reactions, the compositions of the half-charged, first charged, and first discharged states were estimated to be $\text{Li}_{0.77}\text{Ni}_{0.15}\text{Co}_{0.19}\text{Mn}_{0.50}\text{O}_2$, $\text{Li}_{0.11}\text{Ni}_{0.15}\text{Co}_{0.19}\text{Mn}_{0.50}\text{O}_2$ and $\text{Li}_{1.04}\text{Ni}_{0.15}\text{Co}_{0.19}\text{Mn}_{0.50}\text{O}_2$, respectively. Figure S3 (Supporting Information) shows the crystal structures assumed in the PDF analysis. In the pristine and half-charged states, we assumed a two-phase model of the base structure comprising $R\bar{3}m$ and $C2/m$ with the compositions $\text{Li}(\text{Ni}_{1/3}\text{Co}_{1/3}\text{Mn}_{1/3})\text{O}_2$ and Li_2MnO_3 , respectively. A single-phase model considering the $R\bar{3}m$ structure of Li_xMeO_2 was applied for the charged and discharged states, because of the loss of the superlattice peaks of $C2/m$. The occupation of the tetrahedral Li site by the transition metal (Ni ions in this analysis) in the $R\bar{3}m$

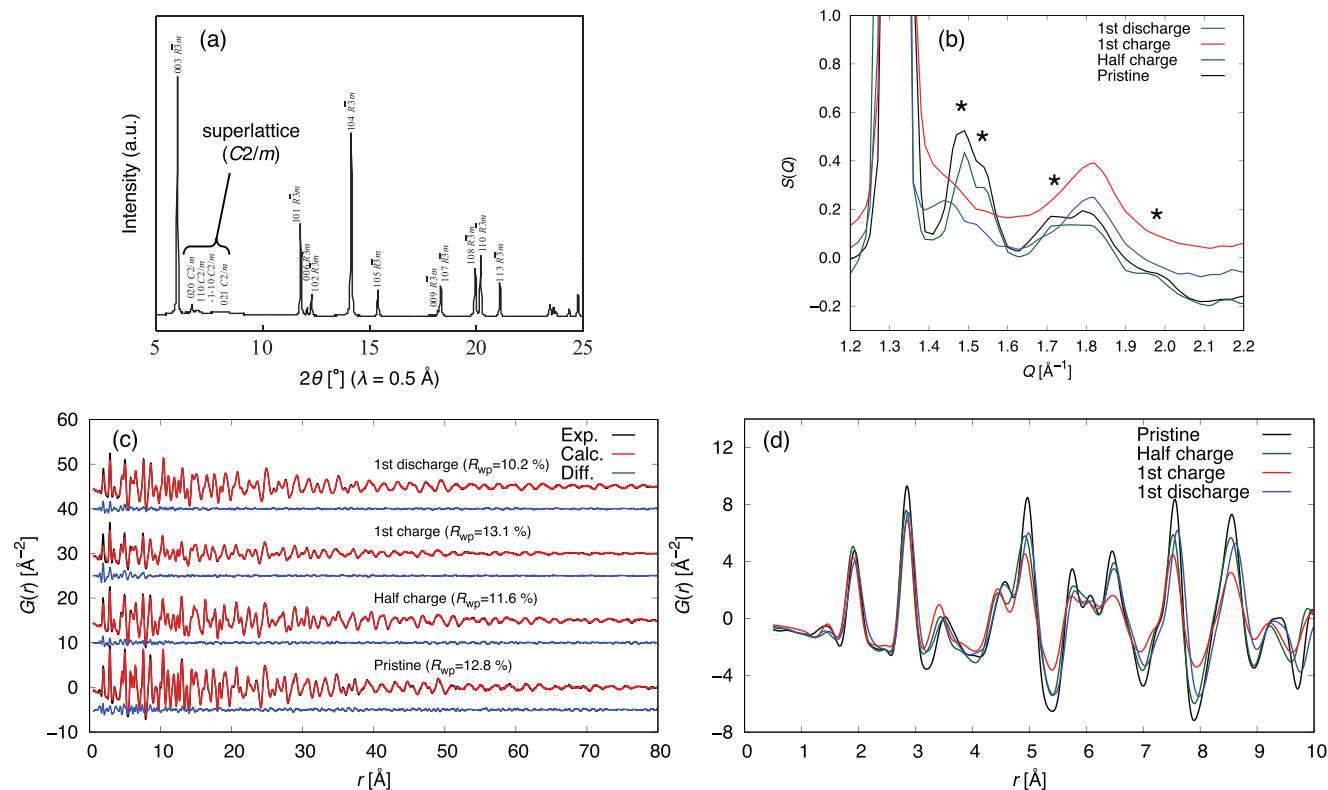


Figure 2. a) High-resolution XRD profile for the pristine $\text{Li}_{1.16}\text{Ni}_{0.15}\text{Co}_{0.19}\text{Mn}_{0.50}\text{O}_2$ obtained at the beamline BL19B2 in SPring-8. The Miller indices are given in the space group symmetry of $R\bar{3}m$. b) Superlattice peaks of the experimental structure factors, $S(Q)$. The asterisks correspond to the superlattice peaks from $C2/m$. c) Experimental (black) and calculated (red) $G(r)$ of electrode samples. The blue curves correspond to the difference. R_{wp} was calculated in the range of 10–120 Å. d) Experimental $G(r)$ for the various states in the short-range region.

structure was assumed. This tetrahedral site is in the Li layer and located in the middle position of the pathway between the octahedral Me and Li sites, as shown in Figure S3b (Supporting Information). For the refinement of the $R\bar{3}m$ structures, both the octahedral and tetrahedral Li site occupancies were refined, whereas the occupancy of the transition metal in the tetrahedral Li site asymptotically approached 0 for the lithiated states; therefore, it was fixed at 0. The refined results are listed in Table S1 (Supporting Information). X-ray total scattering measurements hardly distinguish the species of transition metals in the composites between Mn, Co, and Ni, as their atomic numbers are close to each other. Therefore, the occupancy of the transition metal was refined assuming only Ni ions out of the transition metals that can migrate between Li and Me sites for simplicity. R_{wp} and the occupancy of the transition metal in the tetrahedral Li site changed little if the Mn ions instead of the Ni or Co ions migrated into the site (Table S2 in Supporting Information). As previously reported, oxygen desorption is known to occur in this system during the initial charging.^[1,5,47,48] However, the O-ion occupancy was fixed at unity for this analysis because there is no significant change in R_{wp} (Table S3, Supporting Information). This result reflects the difficulty of analyzing O, a light element, using the X-ray source.

Crystallographic structural analysis for the positive electrode materials in various states was performed. Rietveld analysis is the most widespread method to refine the structural parameters of crystals. In this study, the structural parameters were refined

by PDF-based structural refinement in the long-range region (10–120 Å) on behalf of the Rietveld analysis. The PDF-based structural refinement has different sensitivity for the structural parameters from the Rietveld analysis. Here, the difference between PDF-based structural refinement and Rietveld analysis will be mentioned before discussing the result of the analysis for the positive electrodes. The occupancy of the transition metal in the crystal is estimated by the intensity ratio of the Bragg peak profile. Figure 3a,b shows the R_{wp} variation effect on the Ni-ion occupancy in the Li tetrahedral site assumed for the charged-state samples. The leaking fraction shown on the x-axis is the ratio of Ni occupancy in the Li tetrahedral site to the total amount of Ni. Note that the scattering intensity used in the analysis, $I_{\text{obs}}(Q)$, contained the background from binder carbon. In the Rietveld analysis, R_{wp} decreased by only 4% when assuming the leakage of transition metal into the Li tetrahedral site. On the other hand, R_{wp} dropped markedly by 36% in the PDF-based structural refinement. This result strongly supports the validity of the transition-metal leaking into the Li tetrahedral site in the $R\bar{3}m$ structure. The different R_{wp} sensitivity to the transition-metal migration is derived from the high accuracy of the calculated Bragg peak intensity because the PDF-based structural refinement can avoid background scattering from amorphous impurity. Since interatomic correlations decay over short distances in the case of amorphous impurities, its contribution is negligible in the long-range region of the PDF. Figure 4a,b shows the fitting results obtained by the Rietveld

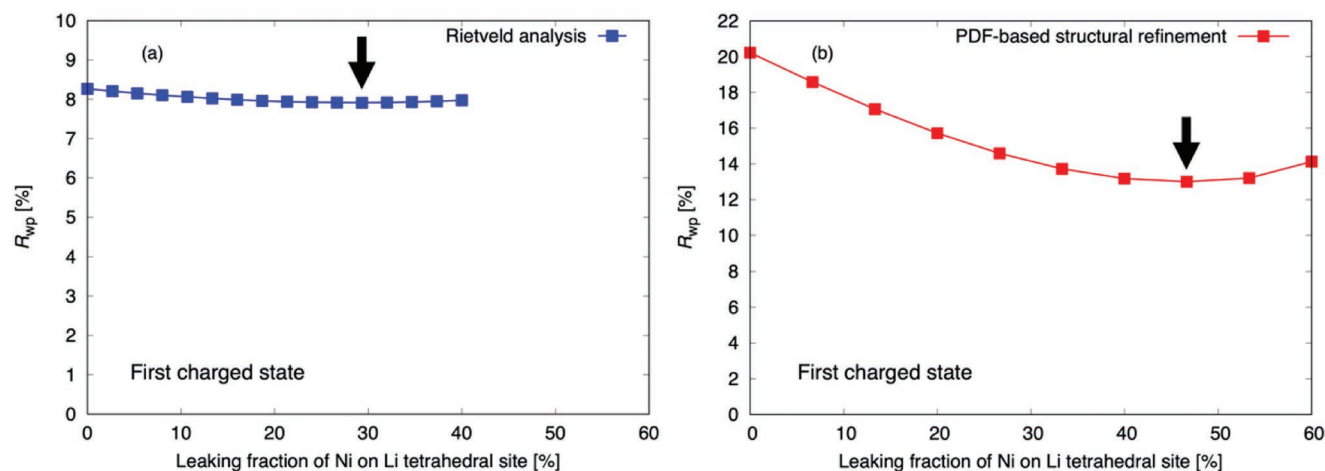


Figure 3. Goodness-of-fit sensitivity to Ni-ion leaking into the Li tetrahedral site in the first charged sample by a) Rietveld analysis and b) PDF-based structural refinement. The arrows correspond to the best condition of the leaking fraction of each analysis.

analysis and PDF-based structural refinement. The improvement of the calculated diffraction pattern by the occupancy refinement is nominal in the Rietveld analysis; consequently, the difference between the calculated results shown in Figure 4a can hardly be recognized. In contrast, the PDF-based structural refinement yields a clear difference in the PDFs in the intermediate region (10–30 Å). It allows us to refine the transition metals in the tetrahedral Li site accurately. Further details of the difference between these analyses can be found in Supporting Information.

The PDF-based structural refinements provided various structural parameters of the crystal structures for the pristine, half-charged, first charged/discharged, and 20th charged/discharged states. Figure 2c shows the fitting results in the long-range region (10–120 Å) for the samples as well as the experimental $G(r)$. The mole ratio of $C2/m$ to $R\bar{3}m$ is 0.405 ($0.3/0.7 = 0.428$) for the pristine material, which consists of $0.3\text{Li}_2\text{MnO}_3$ and $0.7\text{Li}(\text{Ni}_{1/3}\text{Co}_{1/3}\text{Mn}_{1/3})\text{O}_2$, as expected. No significant changes in the domain size and the lattice distortion of the $R\bar{3}m$ phase were confirmed regardless of the state, whereas the lattice constants changed. The lattice constants of the a and

b axes were decreased by delithiation, which is the same trend as in the conventional layered materials and other LLO materials (Figure 5a).^[1,9–11,49–54] The lattice constants of the a/c axes of the $R\bar{3}m$ domain are 2.852/14.235 Å, and those the $a/b/c$ axes of the $C2/m$ domain are 4.919/8.523/5.007 Å, which are similar to the reported lattice parameters of 2.867/14.246 Å^[47] of the single-phase $\text{Li}(\text{Ni}_{1/3}\text{Co}_{1/3}\text{Mn}_{1/3})\text{O}_2$, and 4.932/8.535/5.027 Å^[48] of the single-phase Li_2MnO_3 , respectively. The lattice volume of the $R\bar{3}m$ domain in the half-charged state showed no changes compared with the pristine state; nevertheless, the lattice constants changed. The single-phase $\text{Li}(\text{Ni}_{1/3}\text{Co}_{1/3}\text{Mn}_{1/3})\text{O}_2$ reported by Yabuuchi and Ohzuku also showed the same features before delithiating up to 0.6 mol ($\approx 170 \text{ mAh g}^{-1}$).^[55] In contrast, the variation of the lattice constant of the $C2/m$ domain is very small compared with that of $R\bar{3}m$ upon half-charging. This is consistent with the finding that the Li ions are extracted from the $R\bar{3}m$ domain preferentially before the half-charged state. The shortening of the a and b axes corresponds to the shrinkage of the metal layer involved in the redox reaction of the transition metal ions. On the other hand, the lattice constant along the c axis increased with lithiation and increased

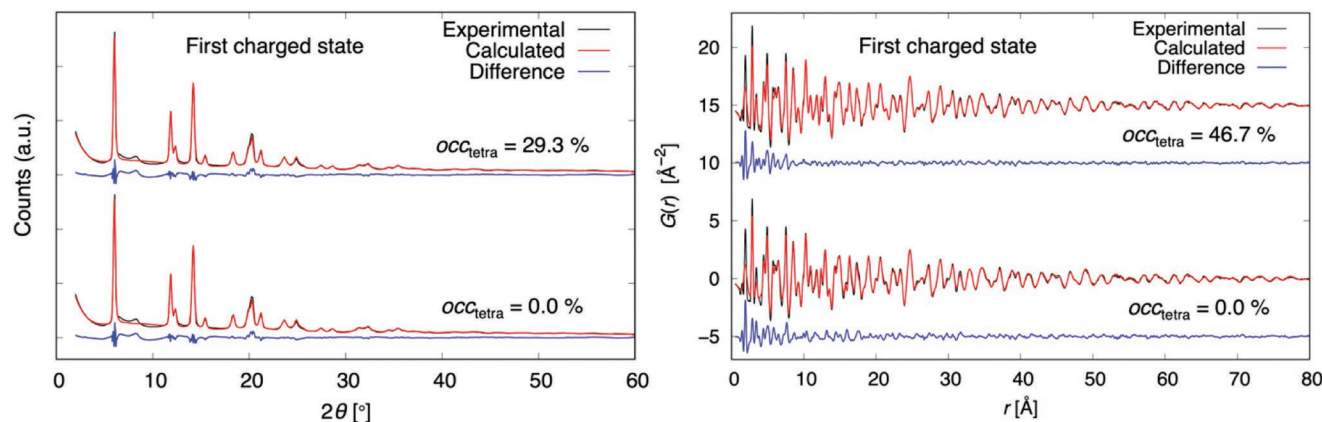


Figure 4. Fitting results depending on the fraction of Ni-ion leaking into the tetrahedral Li site obtained by a) Rietveld analysis and b) PDF-based structural refinement.

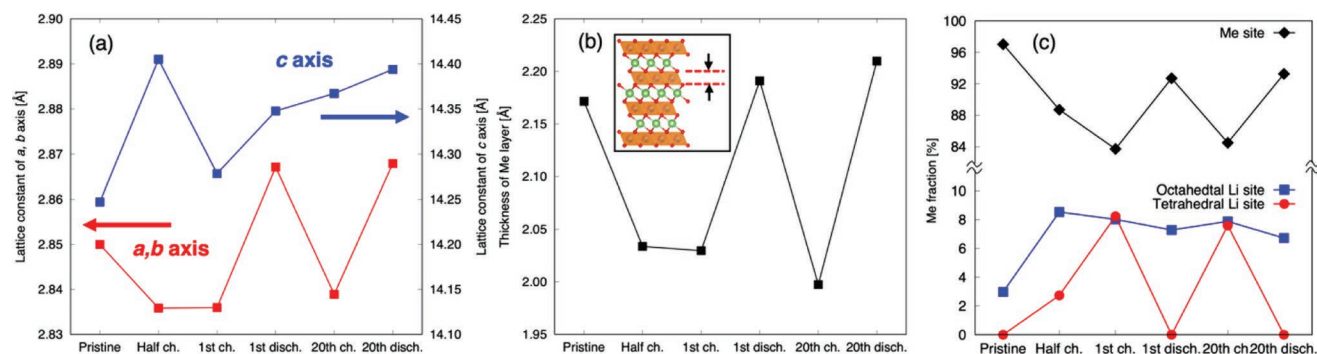


Figure 5. a) Lattice constants of a/b and c axes, b) Me layer thickness and Ni occupancy in the octahedral and tetrahedral Li sites of the $R\bar{3}m$ structure. The inset shows the definition of the Me layer thickness. c) Variation of transition metal fraction with sample state.

cycle number. The variation of the lattice parameters and Me-layer thickness of the $R\bar{3}m$ phase provided evidence of delithiation from $\text{Li}(\text{Ni}_{1/3}\text{Co}_{1/3}\text{Mn}_{1/3})\text{O}_2$. Considering the formation of the single phase of $R\bar{3}m$ in the first charged state, the mixing of the transition metals between the $R\bar{3}m$ and $C2/m$ phases is considered to have occurred after the half-charge. It was found that there was a strong correlation between the Me layer thickness and the lattice constants along with the a and b axes (Figure 5b). The ionic radius of the transition metal decreases upon oxidation to charge-compensate for the delithiation. The occupancy of Li ions and the Me-layer thickness decreased in the half-charged state. These results suggest that Li ions were released from the $R\bar{3}m$ domain, not from the $C2/m$ domain, in the voltage gradient region during the initial charging process. This is consistent with the in situ XAFS results^[6] that the Ni and Co ions in the $\text{Li}_{1.16}\text{Ni}_{0.15}\text{Co}_{0.19}\text{Mn}_{0.50}\text{O}_2$ electrode are oxidized during the initial charging to half-charged states as well as similar to those of the $\text{LiNi}_{1/3}\text{Co}_{1/3}\text{Mn}_{1/3}\text{O}_2$ electrode.

The occupancy of the transition metal in the Li layer showed considerable variation depending on the state. Figure 5c shows the transition metal occupancy variation due to the state of charge/discharge in the $R\bar{3}m$ structure. It is noteworthy that the results of both the Rietveld analysis and PDF-based structural refinement suggest the occupancy of transition metals in the tetrahedral Li site at the delithiated states (Figure 3). The PDF-based structural refinement results clearly show that the transition metal occupies the tetrahedral site of the Li layer in the $R\bar{3}m$ structure. Hence, the PDF-based structural refinement is expected to enable the accurate evaluation of the migration of transition metals. In Figure 5c, the site occupancies are described as the ratio of the amount of Ni ions on the octahedral and tetrahedral sites in the Li layer and the octahedral sites in the Me layer to the total amount of Me ions (Ni, Co, and Mn) in the $R\bar{3}m$ structure. Note again that only the occupancy of Ni ions was refined for simplicity. In the composite pristine material, the $R\bar{3}m$ phase had only a low Me occupancy in the octahedral Li site. In the initial charging process, a different migration of the transition metal ion occurred. The Me occupancy in the octahedral Li site increased by 8.5% in the half-charged state, whereas that in the tetrahedral Li site only slightly increased. This suggests a preferential migration into the octahedral Li site from the Me site. Then, the Me occupancy in the tetrahedral Li site increased to 8.2% at the first charged state, whereas that on the octahedral Li site remained

almost unchanged. Therefore, 16.3% of the Me ions migrated into the Li layer upon delithiation. After the first charge, the transition metals that migrated into the two sites showed different behavior in the subsequent charge and discharge cycles. The occupancy on the octahedral Li site seemed almost unchanged by the cycling. In contrast, the occupancy on the tetrahedral Li site sensitively varied with Li insertion/extraction. No transition metals in the tetrahedral Li site were found to be in the discharged state because the metals transferred back to the Me site upon lithiation. Therefore, the reversible migration of the transition metals associated with delithiation and lithiation occurs mainly between the Me and tetrahedral sites. Transition metal ions in octahedral Li sites generally act as pillars to support the vacant Li layers and prevent the breakdown of the layered structure upon delithiation. However, the pillars will inhibit the Li-ion diffusion during the charging process.^[53,56] These transition metal ions in the octahedral Li sites act as rigid pillars independent of the Li-ion concentration. On the other hand, the transition metal ions in the tetrahedral Li sites act as adaptive pillars, which change with the Li-ion concentration in the Li layers during the charge and discharge process because the metals easily move back to the Me site. Therefore, the transition metals in both the tetrahedral and octahedral Li sites support the vacant Li layers in the charged state. In contrast, the transition metals in the tetrahedral site move back to the Me site when the Li-ion concentration increases upon discharging. The transition metals acting as adaptive pillars contribute to the higher reversible capacity, resulting in two advantages; stabilization of the structure in the charged state and accommodation of large amounts of Li ions in the Li layer in the discharged state through migration back to the Me site. Observed unique migration of the transition metal elements could participate in the correlation between Me layers. The c -axis lattice constant had different variations to the charge–discharge process compared to the other lattice constants and the Me-layer thickness as shown in Figure 5a,b. This trend obviously suggests that the Li layer becomes thicker with increasing cycle number. The rigid pillars and adaptive pillars formed in the Li layer will be an origin of the c -axis lattice constant variation. However, cycle number dependency of the number of pillars was not able to reasonably explain the Li-layer expansion. Perhaps, the species of the transition metal element or localization of the pillars might be involved in the variation. Unfortunately, the origin was not confirmed in this

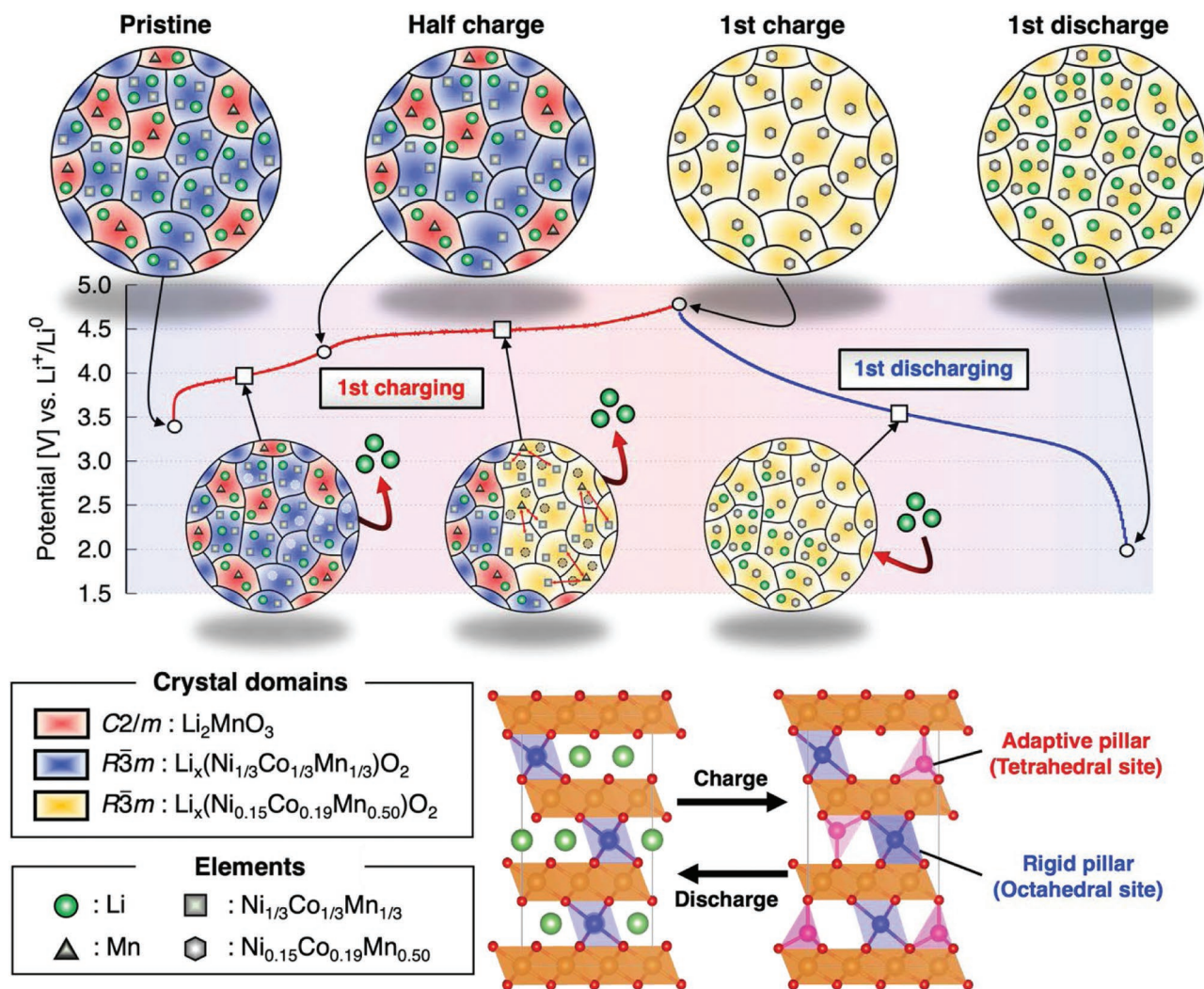


Figure 6. Schematic illustration of the crystal structures during the charge–discharge process for $\text{Li}_{1.16}\text{Ni}_{0.15}\text{Co}_{0.19}\text{Mn}_{0.50}\text{O}_2$. Red, blue, and yellow cells indicate the crystalline domains of Li_2MnO_3 , $\text{Li}_x(\text{Ni}_{1/3}\text{Co}_{1/3}\text{Mn}_{1/3})\text{O}_2$, and $\text{Li}_x(\text{Ni}_{0.15}\text{Co}_{0.19}\text{Mn}_{0.50})\text{O}_2$ -based structures in a primary particle, respectively. During the delithiation, the Me ions in the Li_2MnO_3 and $\text{Li}_x(\text{Ni}_{1/3}\text{Co}_{1/3}\text{Mn}_{1/3})\text{O}_2$ domains migrate between the two domains and form a new $R\bar{3}m$ domain. Two kinds of pillar in the new $R\bar{3}m$ domain are also illustrated.^[63] The adaptive pillars support the Li layer together with the rigid pillar at the charged state.

study because the Ni, Co, and Mn elements were difficult to identify by X-ray.

Capacity fading was observed up to 20 cycles, as shown in Figure 1. Kawaguchi et al.^[57] proposed two degradation modes for enhanced-entropy layered oxides: rapid and slow degradation. The rapid degradation mode is caused by the inhibition of Li diffusion due to the migration of transition metal ions to the octahedral site in the Li layer observed in the first two to three cycles. On the other hand, the slow degradation mode is caused by cation mixing to the tetrahedral sites in the Li layer, which is reversible in the first two to three cycles, but cations slowly accumulate in the Li layer as the number of cycles increases. In the LLO material used in this study, the transition metal occupancy in the octahedral Li site did not change significantly after the first charge process (Figure 5c), indicating that the transition metal in the octahedral site in the Li layer is

immobilized independently of the extraction and insertion of Li ions up to 20 cycles. These immobile metals in the Li layer are partly attributed to the irreversible capacity degradation (rapid degradation) in the initial cycles. On the other hand, we observed no slow degradation behavior of the tetrahedral site up to 20 cycles. Our sample was cycled only to a small number (20 cycles); hence its effects on the slow degradations of the adaptive and/or rigid pillars are not clear. It is important to clarify the effects of rigid and adaptive pillars on cycle degradation to design the next-generation high-capacity cathode materials. Nevertheless, our results showed that the transition metal in the tetrahedral site of the Li layer migrates in response to the extraction and insertion of Li ions, which is the specific structural mechanism behind the high capacity of the LLO material.

Figure 6 shows a schematic diagram of the structural evolution involved in the charge–discharge process for

$\text{Li}_{1.16}\text{Ni}_{0.15}\text{Co}_{0.19}\text{Mn}_{0.50}\text{O}_2$. The initial state of this positive electrode material is considered to be a composite structure of two crystalline domains, the Li_2MnO_3 - and $\text{Li}(\text{Ni}_{1/3}\text{Co}_{1/3}\text{Mn}_{1/3})\text{O}_2$ -based domains, which is not a simple mixture of these phases. Li ions desorb preferentially from the $\text{Li}(\text{Ni}_{1/3}\text{Co}_{1/3}\text{Mn}_{1/3})\text{O}_2$ domain until the half-charged state in the initial charging process. Li ions are only extracted from the $\text{Li}(\text{Ni}_{1/3}\text{Co}_{1/3}\text{Mn}_{1/3})\text{O}_2$ domain up to, at most, 0.6 mol because the volume of the domain does not change in the half-charged state.^[55] Some of the transition metals in the Me site move to the vacant octahedral Li site with decreasing Li-ion concentration. After the half-charged state, a voltage plateau is observed at ≈ 4.5 V in the charge–discharge profile. It is presumed that Li ions are mainly extracted from the Li_2MnO_3 domain during the voltage plateau.^[18] Furthermore, the remaining Li ions in the $\text{Li}(\text{Ni}_{1/3}\text{Co}_{1/3}\text{Mn}_{1/3})\text{O}_2$ domain are simultaneously extracted. In this process, the mixing of the transition metals via the tetrahedral site would proceed. When the Li ions are fully extracted, a new $R\bar{3}m$ structure with a high concentration of Mn ions, $\text{Li}_x\text{Ni}_{0.15}\text{Co}_{0.19}\text{Mn}_{0.50}\text{O}_2$, is formed. There are two Li sites that can be occupied by the transition metals in the $R\bar{3}m$ phase, octahedral and tetrahedral sites. The transition metals in these two sites show different responses to lithiation and delithiation. The transition metals on the octahedral site remain regardless of lithiation/delithiation, whereas the transition metals in the tetrahedral site move back and forth between the tetrahedral site and the Me site depending on the Li-ion concentration. The transition metal on the octahedral site in the Li layer acts as a rigid pillar. The rigid pillar inhibits the diffusion of the Li ions,^[53,56] although this pillar supports the crystal structure during delithiation. By contrast, the transition metal on the tetrahedral site in the Li layer functions as an adaptive pillar. The adaptive pillar supports the empty Li layer together with the rigid pillar in the charged state. When the Li-ion concentration increases upon lithiation, the adaptive pillar vanishes to promote insertion paths for the Li ions. Therefore, the adaptive pillar contributes to both the diffusion of Li ions and the stability of the layered structure. As a result, the extraction and insertion of 1 mol of Li ions can be achieved. Note that we were unable to identify the type of transition metal element among Ni, Mn, and Co contributing to each pillar. It has been reported that the structure of layered oxides in the delithiated state differs depending on the transition metal element. The conventional layered oxide LiCoO_2 and LiNiO_2 retain their layered structure after delithiation,^[51–54] whereas LiMnO_2 changes to a spinel structure.^[58–60] In other words, Ni ions remain in the octahedral sites, whereas Mn ions occupy both octahedral and tetrahedral sites. In metal oxides, Ni^{2+} ions are rarely found in the tetrahedral configuration.^[61] This suggests that Ni and Co ions function as rigid pillars. In LLO materials, Mn is expected to play an essential role in charge compensation during Li desorption/insertion.^[62] Our results suggest that transition metal ions contribute to stabilizing the Li layers that contribute to the extraction and insertion of large amounts of Li ions in the layered structures. Although it is not possible to distinguish the elemental species of Ni, Co, and Mn by PDF-based structural refinement in this study, Mn, which can be present in both tetrahedral and octahedral sites, is playing an important part in the high capacity

of the LLO materials. A promising route to unveil the mechanism behind the enhanced positive electrode properties is to gain an understanding of the role of transition metal elements in $R\bar{3}m$ layer-structured materials.

3. Conclusion

In this study, X-ray total scattering measurements of a Li-rich positive electrode material, $\text{Li}_{1.16}\text{Ni}_{0.15}\text{Co}_{0.19}\text{Mn}_{0.50}\text{O}_2$, were performed. The structural parameters in the various states of charge/discharge were determined through PDF-based structural refinements using experimental $G(r)$. The materials in the pristine and half-charged states were described as a composite of $R\bar{3}m$ and $C2/m$ structures. After the initial charge, a new $R\bar{3}m$ structure was formed by mixing the transition metal ions in the two phases. The transition metal ions that move to the Li sites and function as pillars were elucidated. There are two kinds of pillar sites, octahedral and tetrahedral sites, in the Li layer. The transition metal ions occupying the octahedral site support the crystal structure as rigid pillars because the metal ions stay unchanged during de/lithiation. In contrast, the transition metals occupying the tetrahedral site move back and forth between the tetrahedral site and the Me site. These transition metals act as adaptive pillars. When the amount of Li in the Li layer decreases during delithiation, the transition metals move to the tetrahedral site of the vacant Li layer to function as pillars that support the Li-poor layer. During Li insertion, the transition metals return to the Me layer to facilitate Li insertion to the Li layer, contributing to the high capacity of the positive electrode material. The rigid pillars were almost immobile after the initial charge, which suggests that the rigid pillars are related to the rapid capacity fading. Therefore, the rate and cycle properties of the LLO electrode materials are promised to be improved by designing high-endurance rigid pillars.

4. Experimental Section

Synthesis of the Positive Electrode: $\text{Li}_{1.16}\text{Ni}_{0.15}\text{Co}_{0.19}\text{Mn}_{0.50}\text{O}_2$ was prepared by a solid-state reaction from lithium hydroxide and nickel-cobalt-manganese carbonate.^[6] Nitrate solutions each containing 2 mol dm^{-3} of metal ions in distilled water were prepared from $\text{Ni}(\text{NO}_3)_2 \cdot 6\text{H}_2\text{O}$ (Wako, 99.9%), $\text{Co}(\text{NO}_3)_2 \cdot 6\text{H}_2\text{O}$ (Wako, 99.5%), and $\text{Mn}(\text{NO}_3)_2 \cdot 4\text{H}_2\text{O}$ (Fluka, 97.0%UP). Desired quantities of metal nitrate solutions were added to a 2 mol dm^{-3} Na_2CO_3 aqueous solution. The pH of the mixed solution was controlled between 7 and 8 during the precipitation process. The obtained nickel-cobalt-manganese carbonate precipitate was filtered, washed with distilled water, and dried overnight at room temperature. The precipitate was mixed with $\text{LiOH} \cdot \text{H}_2\text{O}$ (Wako, 98–102%). 2 wt% excess $\text{LiOH} \cdot \text{H}_2\text{O}$ was used to offset any lithium evaporation loss during the next calcination process. The mixed powder was calcined at 1173 K for 12 h in air. The ICP-AES analysis was conducted to determine the composition of the powders. Structural characterizations performed by a powder XRD method (RINT2200, Rigaku) with $\text{Cu-K}\alpha$ (40 kV, 40 mA) confirmed that the obtained material was of a single phase without any obvious impurity phase. Morphology of the pristine powder shown in Figure S6 (Supporting Information) was observed by scanning electron microscopy (SEM, JSM-6390, JEOL Ltd.)

Measurements of Electrochemical Performances: An aluminum-laminated cell was used, which consisted of a positive electrode, a lithium metal foil as a negative and reference electrode, and a porous polypropylene film separator. The positive electrode was fabricated from mixtures composed of an active material (80 wt%), carbon (10 wt%),

and a PVdF binder (10 wt%). The electrolyte was 1 M LiPF₆ in ethylene carbonate/dimethyl carbonate (3:7 ratio by volume). Electrochemical measurements were performed at room temperature on an automatic cycling and data recording system (HJ1001SD8, Hokuto Denko). The charge and discharge current density was 17 mA g⁻¹ with a cutoff voltage of 2.0 to 4.8 V versus Li⁺/Li⁰ at room temperature.

High-Energy X-Ray Total Scattering Measurement: Electrode samples for the XRD and X-ray total scattering measurements were electrochemically prepared at 4.8 V (fully charged state) and at 2.0 V (discharged state) of the 1st and 20th cycles. The cells were disassembled in an argon-filled glove box to obtain the sample powders of positive electrode material. They were rinsed with dimethyl carbonate to remove the electrolyte and dried in a vacuum. The sample powders were loaded and sealed in a 2 mm inner-diameter quartz capillary in a glove box under Ar atmosphere to avoid oxidation. X-ray total scattering measurements of the sample powders were performed at the high-energy X-ray diffraction beamline BL04B2 in SPring-8 (Hyogo, Japan).^[64,65] The incident X-ray beam with an energy of 61.4 keV was monochromated by the Si 220 reflection of a bent monochromator installed in the beamline. The scattered X-ray photons from the sample powders were counted by four CdTe detectors (X-123CdTe, Amptek) and two highly pure Ge solid-state detectors (GL0515, CANBERRA Industries), which were installed every 8°. The measurements were performed at 2θ from 0.3° to 49°; hence, the maximum momentum transfer Q_{max} was approximately 25 Å⁻¹. The coherent X-ray scattering intensity I(Q) was obtained by subtracting the X-ray absorption, the Compton scattering, and the contribution of the quartz capillary from the raw X-ray scattering intensity. The structure factor S(Q) was obtained by normalizing I(Q):

$$S(Q) = \frac{I(Q) - \langle |f(Q)|^2 \rangle}{\langle |f(Q)|^2 \rangle} + 1 \quad (1)$$

where $\langle f^2(Q) \rangle = \sum_j c_j |f_j(Q)|^2$, $\langle f(Q) \rangle = \sum_j c_j f_j(Q)$. c_j and $f_j(Q)$ are the mole fraction and atomic scattering factor of the j -th element in the material, respectively. Figure S7 (Supporting Information) shows the raw data obtained by the total scattering measurement for pristine powder. The error bars were estimated as the square root of the total counts of the scattering X-ray. The PDF, $G(r)$, was calculated by Fourier transform of $S(Q)$:

$$G(r) = \frac{2}{\pi} \int_Q \{S(Q) - 1\} \sin Qr Qr \, dQ \quad (2)$$

The upper limit of the integral was Q_{max} which was determined by the experimental conditions. The sequential analyses were executed with original software for BL04B2 beamline.

PDF-Based Structural Refinement: A PDF-based structural refinement was performed for crystalline materials using the self-made software developed by Hiroi et al.^[66–69] to investigate the atomic structure of the samples. The coherent scattering intensity from a crystalline phase, $I_{\text{calc}}(Q)$, was calculated as

$$I_{\text{calc}}(Q) = \frac{2\pi^2}{NV} \sum_{\tau} \frac{|F(\tau)|^2}{|\tau|^2} R(Q - |\tau|) \quad (3)$$

where N is the number of atoms in the structural model with volume V and $R(Q - |\tau|)$ is the Q -broadening function. The Q -broadening function is determined by the instrumental resolution function and the crystallographic domain size. $F(\tau)$ is the crystal structure factor on the reciprocal lattice point, τ :

$$F(Q) = \sum_j^N f_j(Q) \exp(iQ \cdot r_j) \quad (4)$$

where Q is the reciprocal lattice vector, $Q = |Q|$, $f_j(Q)$ is the atomic scattering factor of the j -th atomic site, and r_j is the atomic position. A Laue monotonic scattering is added to Equation 3 if several elements

occupy the same atomic site in the crystal structure. The structure factor and PDF of the crystalline phase, $S_{\text{calc}}(Q)$ and $G_{\text{calc}}(r)$, can be obtained from Equations 1 and 2 using Equation 3. Average structural parameters of the crystal, i.e., lattice constants, domain size, and occupancies, were refined by fitting $G(r)$ in the long-range region (10–120 Å). This refinement using $G(r)$ for crystalline materials has an advantage over the commonly used Rietveld analysis. This is discussed in detail in Section 2 and Supporting Information. The crystal $G(r)$ calculated by the procedure described above contains the diffuse scattering derived from the atomic thermal vibration and the substitutional disorder. This information is partly merged into the background in the XRD patterns and neglected in the Rietveld methods. One main feature of the PDF-based structural refinement is the processing of all the contributions from the Bragg reflections and the diffuse scattering due to the thermal vibration and substitutional disorder after subtracting the background scattering from the sample container and air. It enables an accurate and sensitive evaluation of the Bragg peak intensity in terms of the occupancy of the elements.

Supporting Information

Supporting Information is available from the Wiley Online Library or from the author.

Acknowledgements

The X-ray total scattering measurements were carried out at SPring-8 under proposals 2018A1172 and 2018B1463. M.O. thanks Prof. Tomoya Kawaguchi (Tohoku University) for fruitful discussion. This work was supported by JSPS KAKENHI Grant numbers 20H02846, 19H05814, and 20K15031. This work was partly supported by the Research and Development Initiative for Scientific Innovation of New Generation Batteries (RISING) project from the New Energy and Industrial Technology Development Organization (NEDO) of Japan. Rietveld analyses were performed using Rietan-FP.^[70]

Conflict of Interest

The authors declare no conflict of interest.

Data Availability Statement

The data that support the findings of this study are available from the corresponding author upon reasonable request.

Keywords

adaptive pillars, cation mixing, Li-rich layered oxides, lithium-ion batteries, pair distribution function, positive electrode materials, X-ray total scattering measurements

Received: June 2, 2022
Revised: July 21, 2022
Published online: September 2, 2022

- [1] Z. Lu, J. R. Dahn, *J. Electrochem. Soc.* **2002**, *149*, A815.
- [2] M. M. Thackeray, S.-H. Kang, C. S. Johnson, J. T. Vaughey, R. Benedek, S. A. Hackney, *J. Mater. Chem.* **2007**, *17*, 3112.
- [3] J. B. Goodenough, Y. Kim, *Chem. Mater.* **2009**, *22*, 587.

- [4] T. Ohzuku, M. Nagayama, K. Tsuji, K. Ariyoshi, *J. Mater. Chem.* **2011**, 21, 10179.
- [5] N. Yabuuchi, K. Yoshii, S.-T. Myung, I. Nakai, S. Komaba, *J. Am. Chem. Soc.* **2011**, 133, 4404.
- [6] M. Oishi, T. Fujimoto, Y. Takanashi, Y. Orikasa, A. Kawamura, T. Ina, H. Yamashige, D. Takamatsu, K. Sato, H. Murayama, H. Tanida, H. Arai, H. Ishii, C. Yogi, I. Watanabe, T. Ohta, A. Mineshige, Y. Uchimoto, Z. Ogumi, *J. Power Sources* **2013**, 222, 45.
- [7] M. Oishi, C. Yogi, I. Watanabe, T. Ohta, Y. Orikasa, Y. Uchimoto, Z. Ogumi, *J. Power Sources* **2015**, 276, 89.
- [8] Z. Lu, D. D. MacNeil, J. R. Dahn, *Electrochem. Solid-State Lett.* **2001**, 4, A191.
- [9] L. Simonin, J.-F. Colin, V. Ranieri, E. Canévet, J.-F. Martin, C. Bourbon, C. Baetz, P. Strobel, L. Daniel, S. Patoux, *J. Mater. Chem.* **2012**, 22, 11316.
- [10] D. Mohanty, S. Kalnaus, R. A. Meisner, K. J. Rhodes, J. Li, E. A. Payzant, D. L. Wood, C. Daniel, *J. Power Sources* **2013**, 229, 239.
- [11] J. Li, R. Shunmugasundaram, R. Doig, J. R. Dahn, *Chem. Mater.* **2016**, 28, 162.
- [12] A. Ito, Y. Sato, T. Sanada, M. Hatano, H. Horie, Y. Ohsawa, *J. Power Sources* **2011**, 196, 6828.
- [13] H. Koga, L. Croguennec, M. Ménétrier, P. Manneziej, F. Weill, C. Delmas, S. Belin, *J. Phys. Chem. C* **2014**, 118, 5700.
- [14] K. Luo, M. R. Roberts, R. Hao, N. Guerrini, D. M. Pickup, Y.-S. Liu, K. Edström, J. Guo, A. v Chadwick, L. C. Duda, P. G. Bruce, *Nat. Chem.* **2016**, 8, 684.
- [15] K. Luo, M. R. Roberts, N. Guerrini, N. Tapia-Ruiz, R. Hao, F. Massel, D. M. Pickup, S. Ramos, Y.-S. Liu, J. Guo, A. v Chadwick, L. C. Duda, P. G. Bruce, *J. Am. Chem. Soc.* **2016**, 138, 11211.
- [16] W. E. Gent, K. Lim, Y. Liang, Q. Li, T. Barnes, S.-J. Ahn, K. H. Stone, M. McIntire, J. Hong, J. H. Song, Y. Li, A. Mehta, S. Ermon, T. Tyliczszak, D. Kilcoyne, D. Vine, J.-H. Park, S.-K. Doo, M. F. Toney, W. Yang, D. Prendergast, W. C. Chueh, *Nat. Commun.* **2017**, 8, 2091.
- [17] J. Xu, M. Sun, R. Qiao, S. E. Renfrew, L. Ma, T. Wu, S. Hwang, D. Nordlund, D. Su, K. Amine, J. Lu, B. D. McCloskey, W. Yang, W. Tong, *Nat. Commun.* **2018**, 9, 947.
- [18] K. Shimoda, K. Yazawa, T. Matsunaga, M. Murakami, K. Yamanaka, T. Ohta, E. Matsubara, Z. Ogumi, T. Abe, *Sci. Rep.* **2020**, 10, 10048.
- [19] A. Boulineau, L. Simonin, J.-F. Colin, E. Canévet, L. Daniel, S. Patoux, *Chem. Mater.* **2012**, 24, 3558.
- [20] M. Gu, I. Belharouak, J. Zheng, H. Wu, J. Xiao, A. Genc, K. Amine, S. Thevuthasan, D. R. Baer, J.-G. Zhang, N. D. Browning, J. Liu, C. Wang, *ACS Nano* **2012**, 7, 760.
- [21] H. Yu, R. Ishikawa, Y.-G. So, N. Shibata, T. Kudo, H. Zhou, Y. Ikuhara, *Angew. Chem., Int. Ed.* **2013**, 52, 5969.
- [22] X. Yu, Y. Lyu, L. Gu, H. Wu, S.-M. Bak, Y. Zhou, K. Amine, S. N. Ehrlich, H. Li, K.-W. Nam, X.-Q. Yang, *Adv. Energy Mater.* **2014**, 4, 1300950.
- [23] K. A. Jarvis, Z. Deng, L. F. Allard, A. Manthiram, P. J. Ferreira, *Chem. Mater.* **2011**, 23, 3614.
- [24] C. Genevois, H. Koga, L. Croguennec, M. Ménétrier, C. Delmas, F. Weill, *J. Phys. Chem. C* **2014**, 119, 75.
- [25] A. K. Shukla, Q. M. Ramasse, C. Ophus, H. Duncan, F. Hage, G. Chen, *Nat. Commun.* **2015**, 6, 8711.
- [26] K. Shimoda, T. Minato, K. Nakanishi, H. Komatsu, T. Matsunaga, H. Tanida, H. Arai, Y. Ukyo, Y. Uchimoto, Z. Ogumi, *J. Mater. Chem. A* **2016**, 4, 5909.
- [27] T. Kawaguchi, M. Sakaida, M. Oishi, T. Ichitsubo, K. Fukuda, S. Toyoda, E. Matsubara, *J. Phys. Chem. C* **2018**, 122, 19298.
- [28] Y. Idemoto, K. Akatsuka, N. Kitamura, *J. Power Sources* **2015**, 299, 280.
- [29] Y. Idemoto, M. Inoue, N. Kitamura, *J. Power Sources* **2014**, 259, 195.
- [30] F. Amalraj, M. Talianker, B. Markovsky, L. Burlaka, N. Leifer, G. Goobes, E. M. Erickson, O. Haik, J. Grinblat, E. Zinigrad, D. Aurbach, J. K. Lampert, J.-Y. Shin, M. Schulz-Dobrick, A. Garsuch, *J. Electrochem. Soc.* **2013**, 160, A2220.
- [31] K. Kleiner, B. Strehle, A. R. Baker, S. J. Day, C. C. Tang, I. Buchberger, F.-F. Chesneau, H. A. Gasteiger, M. Piana, *Chem. Mater.* **2018**, 30, 3656.
- [32] W. Yin, A. Grimaud, G. Rousse, A. M. Abakumov, A. Senyshyn, L. Zhang, S. Trabesinger, A. Iadecola, D. Foix, D. Giaume, J.-M. Tarascon, *Nat. Commun.* **2020**, 11, 1252.
- [33] H. Xie, J. Cui, Z. Yao, X. Ding, Z. Zhang, D. Luo, Z. Lin, *Chem. Eng. J.* **2022**, 427, 131978.
- [34] D. Y. W. Yu, K. Yanagida, Y. Kato, H. Nakamura, *J. Electrochem. Soc.* **2009**, 156, A417.
- [35] S. F. Amalraj, L. Burlaka, C. M. Julien, A. Mauger, D. Kovacheva, M. Talianker, B. Markovsky, D. Aurbach, *Electrochim. Acta* **2014**, 123, 395.
- [36] H. Koga, L. Croguennec, P. Manneziej, M. Ménétrier, F. Weill, L. Bourgeois, M. Duttine, E. Suard, C. Delmas, *J. Phys. Chem. C* **2012**, 116, 13497.
- [37] H. Zheng, X. Han, W. Guo, L. Lin, Q. Xie, P. Liu, W. He, L. Wang, D. L. Peng, *Mater. Today Energy* **2020**, 18, 100518.
- [38] X. Ji, Q. Xia, Y. Xu, H. Feng, P. Wang, Q. Tan, *J. Power Sources* **2021**, 487, 229362.
- [39] P. Rozier, J.-M. Tarascon, *J. Electrochem. Soc.* **2015**, 162, A2490.
- [40] W. He, W. Guo, H. Wu, L. Lin, Q. Liu, X. Han, Q. Xie, P. Liu, H. Zheng, L. Wang, X. Yu, D.-L. Peng, *Adv. Mater.* **2021**, 33, 2005937.
- [41] B. Li, D. Xia, *Adv. Mater.* **2017**, 29, 1701054.
- [42] G. Assat, J.-M. Tarascon, *Nat. Energy* **2018**, 3, 373.
- [43] R. J. Clément, Z. Lun, G. Ceder, *Energy Environ. Sci.* **2020**, 13, 345.
- [44] M. Oishi, K. Shimoda, K. Ohara, D. Kabutan, T. Kawaguchi, Y. Uchimoto, *J. Phys. Chem. C* **2020**, 124, 24081.
- [45] K. M. Wiaderek, O. J. Borkiewicz, E. Castillo-Martínez, R. Robert, N. Pereira, G. G. Amatucci, C. P. Grey, P. J. Chupas, K. W. Chapman, *J. Am. Chem. Soc.* **2013**, 135, 4070.
- [46] W. Hua, S. Wang, M. Knapp, S. J. Leake, A. Senyshyn, C. Richter, M. Yavuz, J. R. Binder, C. P. Grey, H. Ehrenberg, S. Indris, B. Schwarz, *Nat. Commun.* **2019**, 10, 5365.
- [47] T. Ohzuku, Y. Makimura, *Chem. Lett.* **2001**, 30, 642.
- [48] C. H. Lei, J. G. Wen, M. Sardela, J. Bareno, I. Petrov, S.-H. Kang, D. P. Abraham, *J. Mater. Sci.* **2009**, 44, 5579.
- [49] A. R. Armstrong, M. Holzapfel, P. Novák, C. S. Johnson, S.-H. Kang, M. M. Thackeray, P. G. Bruce, *J. Am. Chem. Soc.* **2006**, 128, 8694.
- [50] F. la Mantia, F. Rosciano, N. Tran, P. Novák, *J. Electrochem. Soc.* **2009**, 156, A823.
- [51] N. Yabuuchi, Y. Makimura, T. Ohzuku, *J. Electrochem. Soc.* **2007**, 154, A314.
- [52] G. G. Amatucci, J.-M. Tarascon, L. C. Klein, *J. Electrochem. Soc.* **1996**, 143, 1114.
- [53] T. Ohzuku, A. Ueda, M. Nagayama, *J. Electrochem. Soc.* **1993**, 140, 1862.
- [54] H. Arai, S. Okada, Y. Sakurai, J. Yamaki, *Solid State Ionics* **1997**, 95, 275.
- [55] N. Yabuuchi, T. Ohzuku, *J. Power Sources* **2003**, 119, 171.
- [56] T. Kawaguchi, K. Fukuda, K. Tokuda, M. Sakaida, T. Ichitsubo, M. Oishi, E. Matsubara, *Phys. Chem. Chem. Phys.* **2015**, 17, 14064.
- [57] T. Kawaguchi, X. Bian, T. Hatakeyama, H. Li, T. Ichitsubo, *ACS Appl. Energy Mater.* **2022**, 5, 4369.
- [58] Y. Jang, B. Huang, H. Wang, D. R. Sadoway, Y. Chiang, *J. Electrochem. Soc.* **1999**, 146, 3217.
- [59] J. Molenda, M. Ziemnicki, J. Marzec, W. Zajac, M. Molenda, M. Bućko, *J. Power Sources* **2007**, 173, 707.
- [60] S. Kim, X. Ma, S. P. Ong, G. Ceder, *Phys. Chem. Chem. Phys.* **2012**, 14, 15571.

- [61] A. R. West, *Basic Solid State Chemistry*, John Wiley & Sons Ltd, New York **1988**.
- [62] M. Oishi, K. Shimoda, S. Okada, R. Imura, K. Yamanaka, H. Yamashige, H. Mizuguchi, I. Watanabe, Y. Uchimoto, T. Ohta, *Mater. Today Commun.* **2020**, 25, 101673.
- [63] K. Momma, F. Izumi, *J. Appl. Crystallogr.* **2011**, 44, 1272.
- [64] K. Ohara, Y. Onodera, M. Murakami, S. Kohara, *J. Phys.: Condens. Matter* **2021**, 33, 383001.
- [65] M. Isshiki, Y. Ohishi, S. Goto, K. Takeshita, T. Ishikawa, *Nucl. Instrum. Methods Phys. Res., Sect. A* **2001**, 467-468, 663.
- [66] S. Hiroi, K. Ohara, S. Ohuchi, Y. Umetani, T. Kozaki, E. Igaki, O. Sakata, *J. Appl. Crystallogr.* **2020**, 53, 671.
- [67] S. Hiroi, K. Ohara, O. Sakata, *Chem. Mater.* **2021**, 33, 5943.
- [68] A. Møllergård, R. L. McGreevy, *Acta Crystallogr. A* **1999**, 55, 783.
- [69] A. Møllergård, R. L. McGreevy, *Chem. Phys.* **2000**, 261, 267.
- [70] F. Izumi, K. Momma, *Solid State Phenom.* **2007**, 130, 15.